The Astronomical Journal, 137:406–418, 2009 January doi:10.1088/0004-6256/137/1/406


# CHEMICAL DIVERSITY IN HIGH-MASS STAR FORMATION

H. Beuther[1], Q. Zhang[2], E. A. Bergin[3], and T. K. Sridharan[2]
[1] Max-Planck-Institute for Astronomy, Königstuhl 17, 69117 Heidelberg, Germany
[2] Harvard-Smithsonian Center for Astrophysics, 60 Garden Street, Cambridge, MA 02138, USA
[3] University of Michigan, 825 Dennison Building, 500 Church Street, Ann Arbor, MI 48109-1042, USA
*Received 2008 April 22; accepted 2008 October 30; published 2008 December 15*

## ABSTRACT

Massive star formation exhibits an extremely rich chemistry. However, few evolutionary details are known yet, especially at high spatial resolution. Therefore, we synthesize previously published Submillimeter Array high spatial resolution spectral line observations toward four regions of high-mass star formation that are in various evolutionary stages with a range of luminosities. Estimating column densities and comparing the spatially resolved molecular emission allow us to characterize the chemical evolution in more detail. Furthermore, we model the chemical evolution of massive warm molecular cores to be directly compared with the data. The four regions reveal many different characteristics. While some of them, e.g., the detection rate of $CH_3OH$, can be explained by variations of the average gas temperatures, other features are attributed to chemical effects. For example, $C^{34}S$ is observed mainly at the core edges and not toward their centers because of temperature-selective desorption and successive gas-phase chemistry reactions. Most nitrogen-bearing molecules are only found toward the hot molecular cores and not the earlier evolutionary stages, indicating that the formation and excitation of such complex nitrogen-bearing molecules needs significant heating and time to be fully developed. Furthermore, we discuss the observational difficulties to study massive accretion disks in the young deeply embedded phase of massive star formation. The general potential and limitations of such kinds of data sets are discussed, and future directions are outlined. The analysis and modeling of this source sample reveal many interesting features toward a chemical evolutionary sequence. However, it is only an early step, and many observational and theoretical challenges in that field lie ahead.

*Key words:* stars: formation – stars: early type – stars: individual (Orion-KL, G29.96, IRAS 23151+5912, IRAS 05358+3543) – ISM: molecules – ISM: lines and bands – ISM: evolution

*Online-only material:* color figures

## 1. INTRODUCTION

One of the main interests in high-mass star formation research today is a thorough characterization of the expected massive accretion disks (e.g., Yorke & Sonnhalter 2002; Krumholz et al. 2007). Observations of this type require high spatial resolution, and disks have been suggested in numerous systems, although not always with the same tracers (for a recent compilation see Cesaroni et al. 2007). A major complication is the large degree of chemical diversity in these regions. This is seen on large scales in terms of the large number of molecular detections (e.g., Schilke et al. 1997; van Dishoeck & Blake 1998), but in particular, on the small scale (of the order $10^4$ AU and even smaller) where significant chemical differentiation is found (e.g., Beuther et al. 2005a). At present, we are only beginning to decipher the chemical structure of these objects at high spatial resolution, whereas our understanding of the physical properties better allows us to place regions into an evolutionary context (e.g., Beuther et al. 2007a; Zinnecker & Yorke 2007). It is not yet clear how our emerging picture of the physical evolution is related to the observed chemical diversity and evolution.

Various theory groups work on the chemical evolution during massive star formation (e.g., Caselli et al. 1993; Millar et al. 1997; Charnley 1997; Viti et al. 2004; Nomura & Millar 2004; Wakelam et al. 2005; Doty et al. 2002, 2006), and the results are promising. However, the observational database against which these models are tested is still relatively poor. Some single-dish low spatial resolution line surveys toward several sources do exist, but they are all conducted with different spatial resolution and covering different frequency bands (e.g., Blake et al. 1987; MacDonald et al. 1996; Schilke et al. 1997; Hatchell et al. 1998; McCutcheon et al. 2000; van der Tak et al. 2000, 2003; Johnstone et al. 2003; Bisschop et al. 2007). Furthermore, the chemical structure in massive star-forming regions is far from uniform, and at high resolution one observes spatial variations among many species, prominent examples are Orion-KL, W3OH/$H_2O$ or Cepheus A (see e.g., Wright et al. 1996; Wyrowski et al. 1999; Beuther et al. 2005a; Brogan et al. 2007).

Single-dish studies targeted larger source samples at low spatial resolution and described the averaged chemical properties of the target regions (e.g., Hatchell et al. 1998; Bisschop et al. 2007). However, no consistent chemical investigation of a sample of massive star-forming regions exists at high spatial resolution. To obtain an observational census of the chemical evolution at high spatial resolution and to build up a database for chemical evolutionary models of massive star formation, it is important to establish a rather uniformly selected sample of massive star-forming regions in various evolutionary stages. Furthermore, this sample should be observed in the same spectral setup at high spatial resolution. While the former is necessary for a reliable comparison, the latter is crucial to disentangle the chemical spatial variations in the complex massive star-forming regions. Because submm interferometric imaging is a time-consuming task, it is impossible to observe a large sample in a short time. Hence, it is useful to employ synergy effects and observe various sources over a few years in the same spectral lines.

We have undertaken such a chemical survey of massive molecular cores containing high-mass protostars in different

**Table 1**
Source Parameters

| | Orion-KL[b] | G29.96[b] | 23151[b] | 05358[b] |
|---|---|---|---|---|
| $L^{a}$ ($L_{\odot}$) | $10^5$ | $9 \times 10^4$ | $10^5$ | $10^{3.8}$ |
| $d$ (pc) | 450 | 6000 | 5700 | 1800 |
| $M_{gas}{}^{a,c}$ ($M_{\odot}$) | 140[d] | 2500[e] | 600 | 300 |
| $T_{rot}{}^{f}$ (K) | 300 | 340 | 150 | 220 |
| $N_{peak}(H_2)^{g}$ (cm$^{-2}$) | $9 \times 10^{24}$ | $6 \times 10^{24}$ | $2 \times 10^{24}$ | $2 \times 10^{24}$ |
| Type | HMC | HMC | early HMPO | early HMPO |

**Notes.**
[a] Luminosities and masses are derived from single-dish data. Since most regions split up into multiple sources, individual values for submembers are lower.
[b] The SMA data are first published in Beuther et al. (2005a, 2007c, 2007d) and Leurini et al. (2007). Other parameters are taken from Menten & Reid (1995); Olmi et al. (2003); Sridharan et al. (2002); Beuther et al. (2002b).
[c] The integrated masses should be accurate within a factor 5 (Beuther et al. 2002b).
[d] This value was calculated from the 870 $\mu$m flux of Schilke et al. (1997) following Hildebrand (1983) assuming an average temperature of 50 K.
[e] This value was calculated from the 850 $\mu$m flux of Thompson et al. (2006) following Hildebrand (1983) as in comment *b*.
[f] Peak rotational temperatures derived from $CH_3OH$.
[g] $H_2$ column densities toward the peak positions derived from the submm dust continuum observatios (Beuther et al. 2004b, 2007c, 2007d, 2007b).

evolutionary stages using the Submillimeter Array (SMA[4], Ho et al. 2004) since 2003 in exactly the same spectral setup. The four massive star-forming regions span a range of evolutionary stages and luminosities: (1) the prototypical hot molecular core (HMC) Orion-KL (Beuther et al. 2004b, 2005a), (2) an HMC at a larger distance G29.96 (Beuther et al. 2007c), and two regions in a presumably earlier evolutionary phase, namely (3) the younger but similar luminous High-Mass Protostellar Object (HMPO) IRAS 23151+5912 (Beuther et al. 2007d), and (4) the less luminous HMPO IRAS 05358+3543 (Leurini et al. 2007). Although the latter two regions also have central temperatures $>100$ K, qualifying them as "hot," their molecular line emission is considerably weaker than from regions which are usually termed HMCs. Therefore, we refer to them from now on as early HMPOs (see also the evolutionary sequence in Beuther et al. 2007a). Table 1 lists the main physical parameters of the selected target regions.

The SMA offers high spatial resolution (of the order 1″) and a large enough instantaneous bandwidth of 4 GHz to sample numerous molecular transitions simultaneously (e.g., $^{28}$SiO and its rarer isotopologue $^{30}$SiO, a large series of $CH_3OH$ lines in the $v_t = 0, 1, 2$ states, $CH_3CN$, $HCOOCH_3$, SO, $SO_2$, and many more lines in the given setup, see Section 2). Each of these observations has been published separately where we provide detailed discussions of the particularities of each source (Beuther et al. 2004b, 2005a, 2007d; Leurini et al. 2007). These objects span an evolutionary range where the molecular gas and ice-coated grains in close proximity to the forming star are subject to increasing degrees of heating. In this fashion, volatiles will be released from ices near the most evolved (luminous) sources, altering the surrounding gas-phase chemical equilibrium and molecular emission. In this paper, we synthesize these data and effectively re-observe these systems at identical physical resolution in order to identify coherent trends. Our main goals are to search for (a) trends in the chemistry as a function of evolutionary state and (b) to explore, in a unbiased manner, the capability of molecular emission to trace coherent velocity structures that have, in the past, been attributed to Keplerian disks. We will demonstrate that the ability of various tracers to probe the innermost region, where a disk should reside, changes as a function of evolution.

[4] The Submillimeter Array is a joint project between the Smithsonian Astrophysical Observatory and the Academia Sinica Institute of Astronomy and Astrophysics, and is funded by the Smithsonian Institution and the Academia Sinica.

**Table 2**
Spatial Resolution

| | Orion-KL | G29.96 | 23151 | 05358 |
|---|---|---|---|---|
| Cont. (″) | $0.8 \times 0.7$ | $0.4 \times 0.3$ | $0.6 \times 0.5$ | $1.1 \times 0.6$ |
| Av. Cont. (AU) | 340 | 2100 | 3100 | 1500 |
| Line (″) | $1.4 \times 1.1$ | $0.6 \times 0.5$ | $1.1 \times 0.8$ | $1.4 \times 0.8$ |
| Av. Line (AU) | 560 | 3300 | 5400 | 2000 |

## 2. DATA

The four sources were observed with the SMA between 2003 and 2005 in several array configurations achieving (sub)arcsecond spatial resolution. For detailed observational descriptions, see Beuther et al. (2005a, 2007c, 2007d) and Leurini et al. (2007). The main point of interest to be mentioned here is that all four regions were observed in exactly the same spectral setup. The receivers operated in a double-sideband mode with an IF band of 4–6 GHz so that the upper and lower sidebands were separated by 10 GHz. The central frequencies of the upper and lower sidebands were 348.2 and 338.2 GHz, respectively. The correlator had a bandwidth of 2 GHz and the channel spacing was 0.8125 MHz, resulting in a nominal spectral resolution of $\sim$0.7 km s$^{-1}$. However, for the analysis presented below, we smoothed the data cubes to 2 km s$^{-1}$. The spatial resolution of the several datasets is given in Table 2. Line identifications were done in an iterative way: we first compared our data with the single-dish line survey of Orion by Schilke et al. (1997) and then refined the analysis via the molecular spectroscopy catalogs of JPL and the Cologne database of molecular spectroscopy (CDMS; Poynter & Pickett 1985; Mueller et al. 2002).

## 3. RESULTS AND DISCUSSION

### *3.1. Submm Continuum Emission*

To set the four regions spatially into context, Figure 1 presents the four submm continuum images obtained with the SMA. As one expects in a clustered mode of massive star formation, all regions exhibit multiple structures with the number of subsources $\geqslant 2$. As discussed in the corresponding papers, while most of the submm continuum peaks likely correspond to a embedded protostellar sources, this is not necessarily the case for all of them. Some of the submm continuum peaks could be externally heated gas clumps (e.g., the Orion hot-core peak, Beuther et al. 2004b) or may be produced by shock interactions with molecular outflows (e.g., IRAS 05358+3543, Beuther et al. 2007b). In the following spectral line images, we will always show the corresponding submm continuum map in gray scale as a reference frame.

### *3.2. Spectral Characteristics as a Function of Evolution*

Because the four regions are at different distances (Table 1), to compare the overall spectra we smoothed all datasets to the same linear spatial resolution of $\sim$5700 AU. Figure 2 presents the final spectra extracted at this common resolution toward

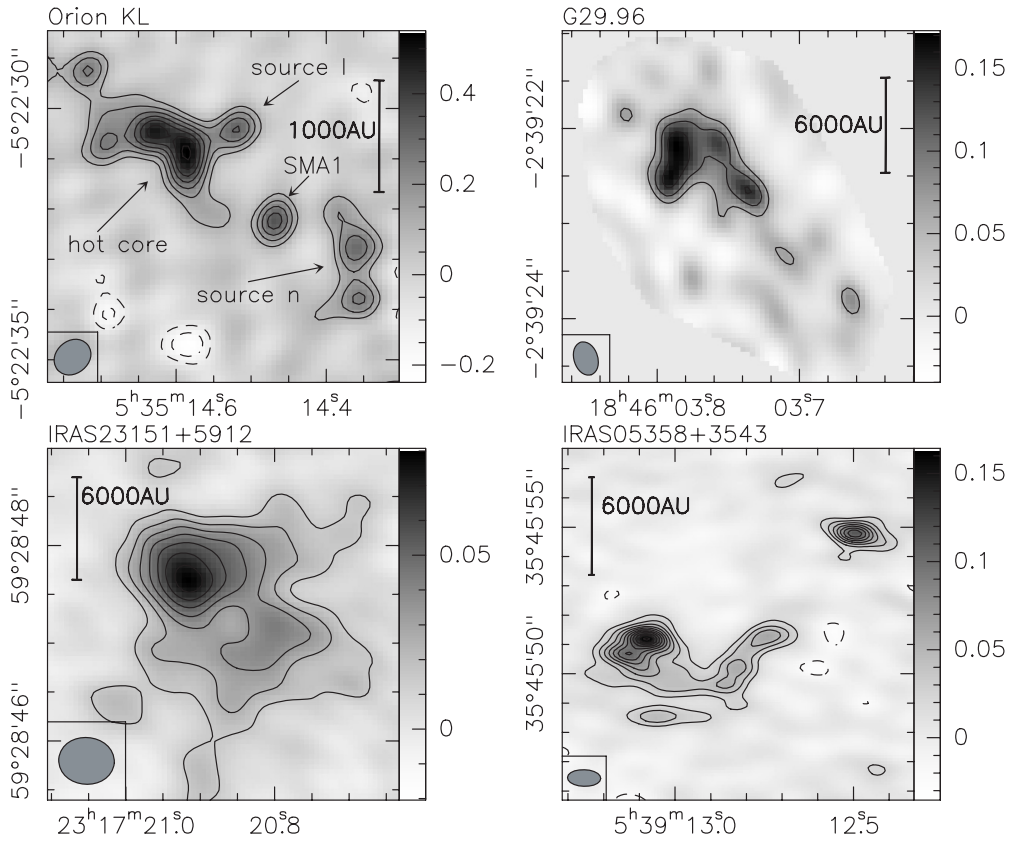


**Figure 1.** 862 $\mu$m continuum images toward the four massive star-forming regions. Positive and negative features are shown as solid and dashed contours, respectively. The contouring always starts at the 3$\sigma$ levels and continues in 2$\sigma$ steps (with 1$\sigma$ values of 35, 21, 5, 7 mJy beam$^{-1}$, respectively). These figures are adaptions from the papers by Beuther et al. (2005a, 2007c, 2007d, 2007b). Scale-bars are presented in each panel, and the wedges show the flux density scales in Jy. The axes are labeled in R.A. (J2000) and decl. (J2000). The synthesized beam sizes are listed in Table 2.

the peak positions of all four regions. Furthermore, we present images at the original spatial resolution of the four molecular species or vibrationally torsionally excited lines that are detected toward all the four target regions (Figures 3–6).

The spectral characteristics between the HMCs and the early HMPOs vary considerably. Table 4 lists all detected lines in the four regions with their upper energy levels $E_u/k$ and peak intensities $S_{\rm peak}$ at a spatial resolution of ∼5700 AU.

### 3.2.1. Excitation and Optical Depth Effects?

Since the line detections and intensities are affected by not only the chemistry but also excitation effects, we have to estimate quantitatively how much the latter can influence our data. In local thermodynamic equilibrium, the line intensities are to first order depending on the Boltzmann factor $e^{\frac{-E_u}{kT}}$ and the partition function $Q$:

$$\int I(T)\,dv \propto \frac{e^{\frac{-E_u}{kT}}}{Q(t)},$$

where $\frac{E_u}{k}$ is the upper level energy state. For polyatomic molecules in the high temperature limit, one can approximate $Q(T) \propto \sqrt{T^3}$ (e.g., Blake et al. 1987). To get a feeling how much temperature changes affect lines with different $\frac{E_u}{k}$, one can form the ratio of $\int I(T)dv$ at two different temperatures:

$$\frac{\int I(2T)\,dv}{\int I(T)\,dv} = \frac{\sqrt{e^{\frac{E_u}{kT}}}}{\sqrt{2^3}}.$$

Equating this ratio now for a few respective upper level energy states and gas temperatures of $T = 100$ & 50 K (Table 3), we find that the induced intensity changes mostly barely exceed a factor 2. Only for very highly excited lines like $CH_3OH(7_{1,7} - 6_{1,6})v_t = 1$ at relatively low temperatures ($T = 50$ K) excitation effects become significant. However, at such low temperatures, these highly excited lines emit well below our detection limits; hence, this case is not important for the present comparison. Therefore, excitation plays only a minor role in producing the molecular line differences discussed below, and other effects like the chemistry turn out to be far more important.

As shown in Table 4, our spectral setup barely contains few lines from rarer isotopologues. We therefore cannot readily determine the optical depth of the molecular lines. While it is likely that, for example, the ground-state $CH_3OH$ lines have significant optical depths, rarer species and vibrationally excited lines should be more optically thin. We checked this for a few respective species (e.g., $C^{34}S$ or $SO_2$) via running large-velocity gradient models (LVG; van der Tak et al. 2007) with typical parameters for these kind of regions, confirming the overall validity of optically thin emission for most lines (see Sections 3.2.2 & 3.2.4). However, without additional data, we cannot address this issue in more detail.

### 3.2.2. Column Densities

Estimating reliable molecular column densities and/or abundances is a relatively difficult task for interferometric datasets

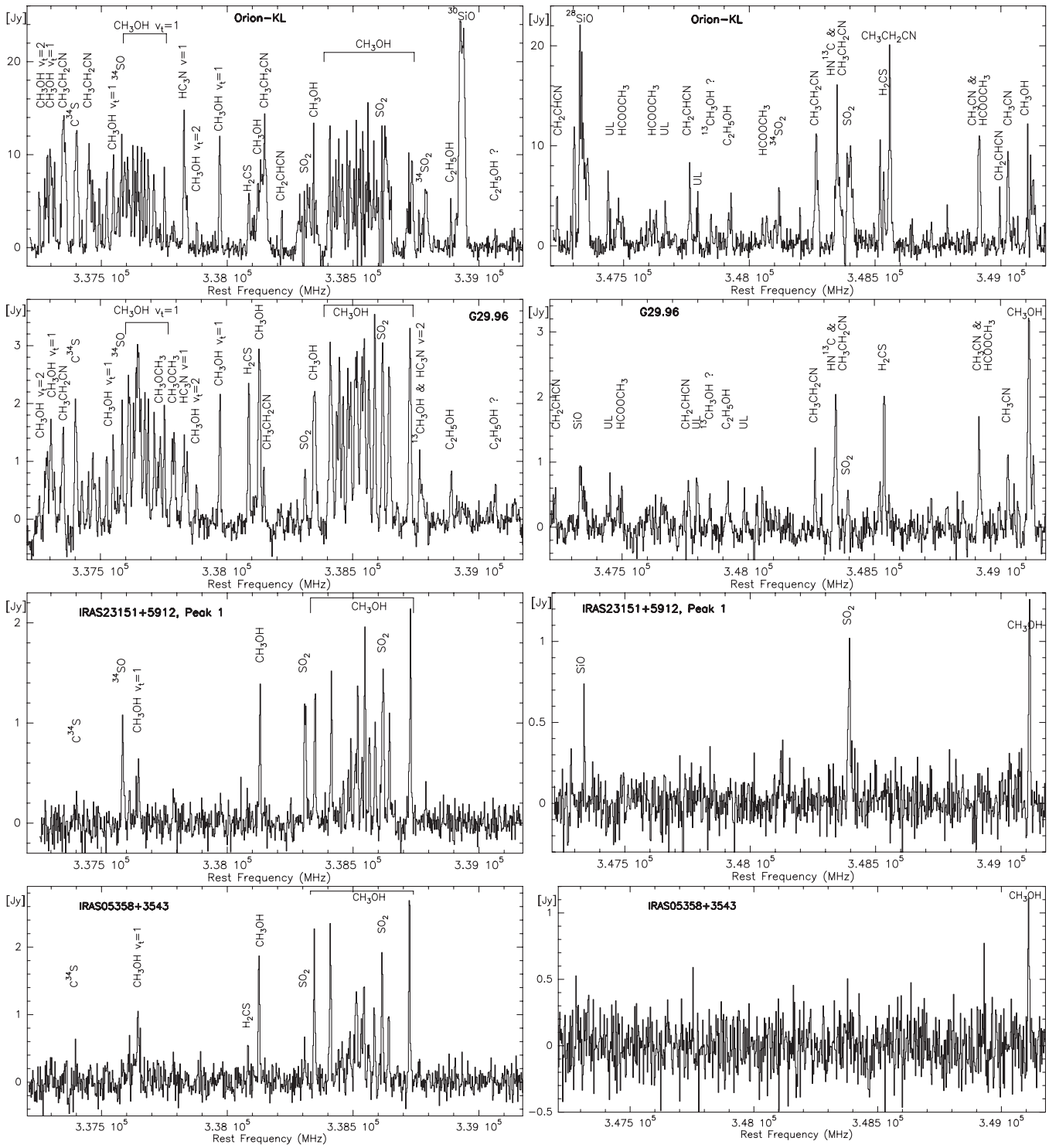


**Figure 2.** SMA spectra extracted from the final data cubes in the image domain toward four massive star-forming regions (Orion-KL top-row, G29.96 second row, IRAS 23151+5912 third row, and IRAS 05358+3543 fourth row). For a better comparison, the data cubes were all smoothed to the same spatial resolution of ∼5700 AU from the current IRAS 23151+3543 dataset. The circles in Figure 3 outline the corresponding spatial regions. The spectral resolution in all spectra is 2 km $s^{-1}$.

like those presented here. The data are suffering from missing short spacings and filter out large fractions of the gas and dust emission. Because of the different nature of the sources and their varying distances, the spatial filtering affects each dataset in a different way. Furthermore, because of spatial variations between the molecular gas distributions and the dust emission representing the $H_2$ column densities, the spatial filtering affects the dust continuum and the spectral line emission differently. On top of this, Figures 3–6 show that in several cases the molecular line and dust continuum emission are even spatially offset, preventing the estimation of reliable abundances.

While these problems make direct abundance estimates relative to $H_2$ impossible, nevertheless, we are at least able to estimate approximate molecular column densities for the sources. Since we are dealing with high-density regions, we can derive

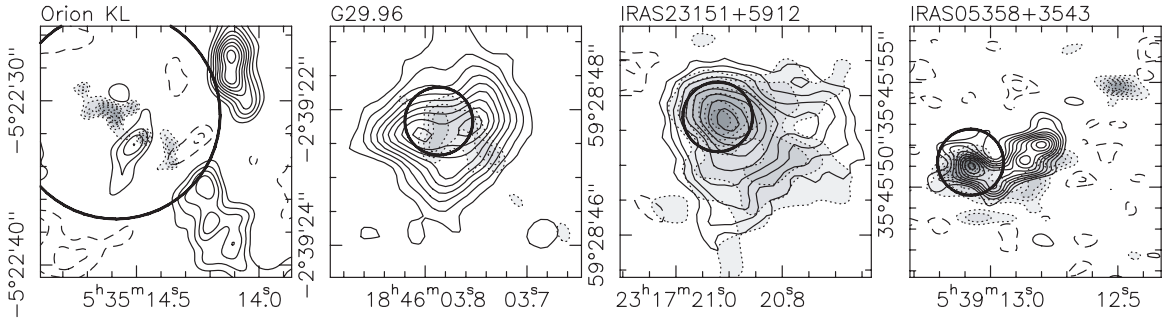


**Figure 3.** $CH_3OH$ contour images (line blend between $CH_3OH(7_{2,5} - 6_{2,4})$ and $CH_3OH(7_{2,6} - 6_{2,5})$) toward the four massive star-forming regions. Positive and negative features are shown as solid and dashed contours. The contouring is done from 15% to 95% (step 10%) of the peak emission, and the peak emission values are 7.5, 0.9, 1.0, and 0.6 Jy beam$^{-1}$ from left to right, respectively. The integration regimes for the four sources are [5,15], [90,104], [−60,−52] and [−20,−12] km s$^{-1}$. The gray scale with dotted contours shows the submm continuum emission from Figure 1. This figure is an adaption from the papers by Beuther et al. (2005a, 2007c, 2007d); Leurini et al. (2007). The axes are labeled in R.A. (J2000) and decl. (J2000). The spatial resolution is listed in Table 2. The circles represent the regions of diameter 5700 AU used for the comparison spectra in Figure 2.

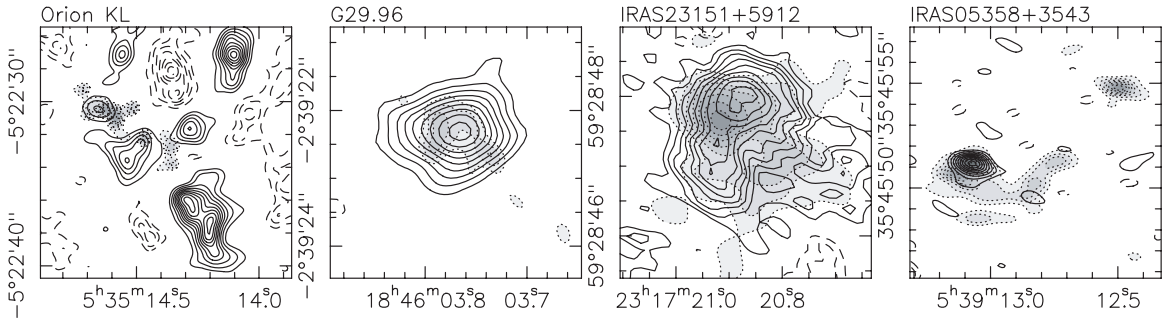


**Figure 4.** Rotationally torsionally excited $CH_3OH(7_{1,7} - 6_{1,6})(v_t = 1)$ images toward the four massive star-forming regions. Positive and negative features are shown as solid and dashed contours. The contouring is done from 15% to 95% (step 10%) of the peak emission, and the peak emission values are 7.5, 0.9, 1.0, and 0.6 Jy beam$^{-1}$ from left to right, respectively. The integration regimes for the four sources are [3,13], [91,105], [−58,−54] and [−18,−10] km s$^{-1}$. The gray scale with dotted contours shows the submm continuum emission from Figure 1. This figure is an adaption from the papers by Beuther et al. (2005a, 2007c, 2007d); Leurini et al. (2007). The axes are labeled in R.A. (J2000) and decl. (J2000). The spatial resolution is listed in Table 2.

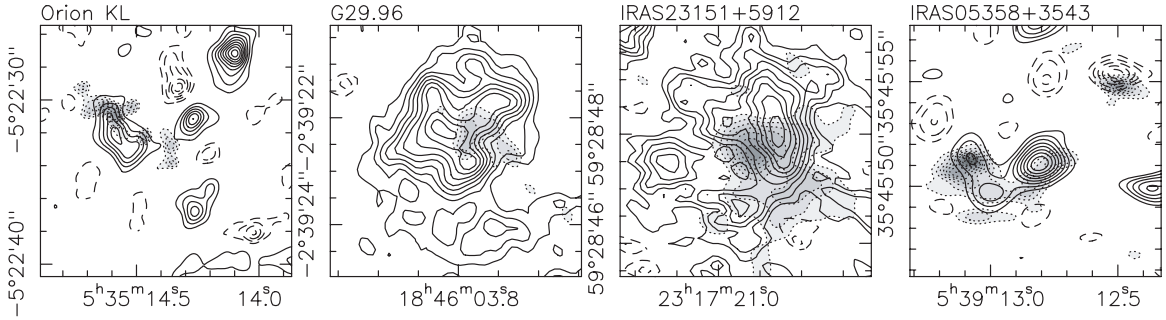


**Figure 5.** $C^{34}S(7–6)$ images toward the four massive star-forming regions. Positive and negative features are shown as solid and dashed contours. The contouring is done from 15% to 95% (step 10%) of the peak emission, and the peak emission values are 7.5, 0.9, 1.0, and 0.6 Jy beam$^{-1}$ from left to right, respectively. The integration regimes for the four sources are [−2,14], [92,104], [−58,−51] and [−17,−13] km s$^{-1}$. The gray scale with dotted contours shows the submm continuum emission from Figure 1. This figure is an adaption from the papers by Beuther et al. (2005a, 2007c, 2007d); Leurini at el. (2007). The axes are labeled in R.A. (J2000) and decl. (J2000). The spatial resolution is listed in Table 2.

the column densities from the spectra shown in Figure 2, assuming local thermodynamic equilibrium (LTE) and optically thin emission. We modeled the molecular emission of each species separately using the XCLASS superset to the CLASS software developed by P. Schilke (2008, private communication). This software package uses the line catalogs from JPL and CDMS (Poynter & Pickett 1985; Müller et al. 2001). The main free parameters for the molecular spectra are temperature, source size, and column density. We used the temperatures given in Table 1 (except of Orion-KL, where we used 200 K because of the large smoothing to 5700 AU) with approximate source sizes estimated from the dust continuum and spectral line maps. Then we produced model spectra with the column density as the remaining free parameter. Considering the missing flux and the uncertainties for temperatures and source sizes, the derived column densities should be taken with caution and only be considered as order of magnitude estimates. Table 5 presents the results for all sources and detected molecules.

### *3.2.3. General Differences*

An obvious difference between the four regions is the large line forest observed toward the two HMCs Orion-KL and G29.96 and the progressively less detected molecular lines toward IRAS 23151+5912 and IRAS 05358+3543. Especially

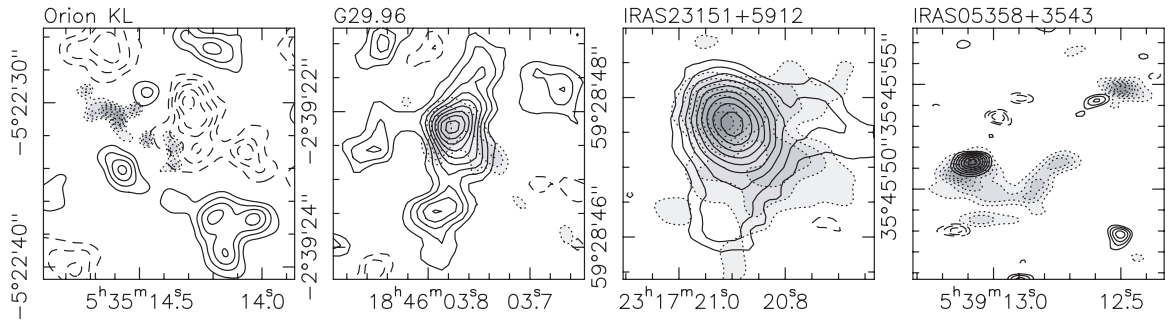


**Figure 6.** $SO_2(14_{4,14}18_{3,15})$ images toward the four massive star-forming regions. Positive and negative features are shown as solid and dashed contours. The contouring is done from 15% to 95% (step 10%) of the peak emission, and the peak emission values are 7.5, 0.9, 1.0, and 0.6 Jy beam$^{-1}$ from left to right, respectively. Only for IRAS 05358+1732 the contouring starts at the 35% level because of a worse signal-to-noise ratio. The integration regimes for the four sources are [0,20], [94,100], [−60,−50] and [−17,−13] km s$^{-1}$. The gray scale with dotted contours shows the submm continuum emission from Figure 1. This figure is an adaption from the papers by Beuther et al. (2005a, 2007c, 2007d) and Leurini et al. (2007). The axes are labeled in R.A. (J2000) and decl. (J2000). The spatial resolution is listed in Table 2.

**Table 3**
Excitation Effects

| Line | $\frac{E_u}{k}$ (K) | $\frac{\int I(2T)dv}{\int I(T)dv}$ @ $T = 100$ K | $\frac{\int I(2T)dv}{\int I(T)dv}$ @ $T = 50$ K |
|---|---|---|---|
| $C^{34}S(7–6)$ | 65 | 0.49 | 0.68 |
| $SO_2(18_{4,1} - 18_{3,1})$ | 197 | 0.95 | 2.5 |
| $CH_3OH(7_{1,7} - 6_{1,6})v_t = 1$ | 356 | 2.1 | 12.4 |

prominent is the difference in vibrationally torsionally excited $CH_3OH$ lines: we detect many transitions in the HMCs and only a single one in the two early HMPOs. Since the vibrationally torsionally excited $CH_3OH$ lines have higher excitation levels $E_u/k$, this can be relatively easily explained by on average lower temperatures of the molecular gas in the early HMPOs. Assuming an evolutionary sequence, we anticipate that the two early HMPOs will eventually develop similar line forests like the two HMCs.

Analyzing the spatial distribution of $CH_3OH$, we find that it is associated with several physical entities (Figures 3 and 4). While it shows strong emission toward most submm continuum peaks, it exhibits additional interesting features. For example, the double-peaked structure in G29.96 (Figure 3) may be caused by a high optical depth of the molecular emission, whereas the lower optical depth vibrationally torsionally excited lines do peak toward the central dust and gas core (Figure 4, smoothing the submm continuum map to the lower spatial resolution of the line data, the four submm sources merge into one central peak). In contrast, toward Orion-KL the strongest $CH_3OH$ features in the ground state and the vibrationally torsionally excited states are toward the southwestern region called the compact ridge. This is the interface between a molecular outflow and the ambient gas. Our data confirm previous work which suggests an abundance enrichment (e.g., Blake et al. 1987). For instance, in quiescent gas in Orion the ratio of $CH_3OH/C^{34}S < 20$ (Bergin & Langer 1997), while our data find a ratio of 100 (see Table 5). This is believed to be caused by outflow shock processes in the dense surrounding gas (e.g., Wright et al. 1996). Furthermore, as will be discussed in Section 3.3, there exist observational indications in two of the sources (IRAS 23151+5912 and IRAS 05358+3543) that the vibrationally torsionally excited $CH_3OH$ may be a suitable tracer of inner rotating disk or tori structures.

Toward G29.96, we detect most lines previously also observed toward Orion-KL, a few exceptions are the $^{30}SiO$ line, some of the vibrationally torsionally excited $v_t = 2$ $CH_3OH$ lines, some N-bearing molecular lines from larger molecules like $CH_3CH_2CN$ or $CH_3CHCN$, as well as a few $^{34}SO_2$ and $HCOOCH_3$ lines. While for some of the weaker lines this difference may partly be attributed to the larger distance of G29.96, for other lines such an argument is unlikely to hold. For example, the $CH_3CH_2CN$ line at 348.55 GHz is stronger than the neighboring $H_2CS$ line in Orion-KL, whereas it remains undetected in G29.96 compared to the strong $H_2CS$ line there. This is also reflected in the different abundance ratio of $CH_3CH_2CN/H_2CS$ which is more than an order of magnitude larger in Orion-KL compared with G29.96 (see Table 5). Therefore, these differences are likely tracing true chemical variations between sources. In contrast, the only lines observed toward G29.96 but not detected toward Orion-KL are a few $CH_3OCH_3$ lines.

The main SiO isotopologue $^{28}SiO(8–7)$ is detected in all sources but IRAS 05358+3543. This is relatively surprising because SiO(2–1) is strong in this region (Beuther et al. 2002a), and the upper level energy of the $J = 8 - 7$ transition of ∼75 K does not seem that extraordinarily high to produce a nondetection. For example, the detected $CH_3OH(7_{1,7} - 6_{1,6})v_t = 1$ transition has an upper level energy of 356 K. This implies that IRAS 05358+3543 does have warm molecular gas close to the central sources. However, the outflow components traced by SiO are at on average lower temperatures (probably of the order 30 K, e.g., Cabrit & Bertout 1990) which may be the cause of the non detection in IRAS 05358+3543. Furthermore, the critical density of the SiO(8–7) line is about two orders of magnitude higher than that of the (2–1) transition. Hence, the density structure of the core may cause the (8–7) nondetection in IRAS 05358+3543 as well.

While the rarer $^{30}SiO(8–7)$ isotopologue is detected toward Orion-KL with nearly comparable strength as the main isotopologue (Figure 2; Beuther et al. 2005a), we do not detect it in any of the other sources.

A little bit surprising, the $H_2CS$ line at 338.081 GHz is detected toward Orion-KL, G29.96 as well as the lowest luminosity source IRAS 05358+3543; however, it remains undetected toward the more luminous HMPO IRAS 23151+5912. We are currently lacking a good explanation for this phenomenon because $H_2CS$ is predicted by most chemistry networks as a parent molecule to be found early in the evolutionary sequence (e.g., Nomura & Millar 2004). The sulfur and nitrogen chemistries are also peculiar in this sample, and we outline some examples below.

**Table 4**
Line Peak Intensities $S_{peak}$ and Upper State Energy Levels $E_u/k$ from Spectra Toward Peak Positions of the Respective Massive Star-forming Regions (Figure 2)

| Freq. (GHz) | Line | $E_u/k$ (K) | $S_{peak}$ (Jy) Orion | $S_{peak}$ (Jy) G29.96 | $S_{peak}$ (Jy) 23151 | $S_{peak}$ (Jy) 05358 |
|---|---|---|---|---|---|---|
| 337.252 | $CH_3OH(7_{3,5} - 6_{3,4})A(v_t = 2)$ | 739 | 6.0 | | | |
| 337.274 | $CH_3OH(7_{4,3} - 6_{4,2})A(v_t = 2)$ | 695 | 7.4 | | | |
| 337.279 | $CH_3OH(7_{2,5} - 6_{2,4})E(v_t = 2)$ | 727 | 5.4 | | | |
| 337.284 | $CH_3OH(7_{0,7} - 6_{0,6})A(v_t = 2)$ | 589 | 9.9 | | | |
| 337.297 | $CH_3OH(7_{1,7} - 6_{1,6})A(v_t = 1)$ | 390 | 10.6 | 1.7 | | |
| 337.312 | $CH_3OH(7_{1,6} - 6_{1,5})E(v_t = 2)$ | 613 | 9.2 | | | |
| 337.348 | $CH_3CH_2CN(38_{3,36} - 37_{3,35})$ | 328 | 14.2 | 1.5 | | |
| 337.397 | $C^{34}S(7–6)$ | 65 | 12.6 | 2.0 | 0.3 | 0.6 |
| 337.421 | $CH_3OCH_3(21_{2,19} - 20_{3,18})$ | 220 | 3.0 | 0.6 | | |
| 337.446 | $CH_3CH_2CN(37_{4,33} - 36_{4,32})$ | 322 | 11.2 | 0.8 | | |
| 337.464 | $CH_3OH(7_{6,1} - 6_{0,0})A(v_t = 1)$ | 533 | 7.2 | 1.1 | | |
| 337.474 | UL | | 4.9 | 0.6 | | |
| 337.490 | $HCOOCH_3(27_{8,20} - 26_{8,19})E$ | 267 | 6.3 | 0.7 | | |
| 337.519 | $CH_3OH(7_{5,2} - 6_{5,2})E(v_t = 1)$ | 482 | 8.1 | 1.0 | | |
| 337.546 | $CH_3OH(7_{5,3} - 6_{5,2})A(v_t = 1)$ | 485 | 10.0[b] | 1.4[b] | | |
| | $CH_3OH(7_{5,2} - 6_{5,1})A^-(v_t = 1)$ | 485 | 10.0[b] | 1.4[b] | | |
| 337.582 | $^{34}SO(8_8 - 7_7)$ | 86 | 12.2 | 2.0 | 1.1 | |
| 337.605 | $CH_3OH(7_{2,5} - 6_{2,4})E(v_t = 1)$ | 429 | 9.7 | 2.4 | | |
| 337.611 | $CH_3OH(7_{6,1} - 6_{6,0})E(v_t = 1)$ | 657 | 6.2[b] | 2.0[b] | | |
| | $CH_3OH(7_{3,4} - 6_{3,3})E(v_t = 1)$ | 388 | 6.2[b] | 2.0[b] | | |
| 337.626 | $CH_3OH(7_{2,5} - 6_{2,4})A(v_t = 1)$ | 364 | 11.0 | 1.9 | | |
| 337.636 | $CH_3OH(7_{2,6} - 6_{2,5})A^-(v_t = 1)$ | 364 | 8.2 | 2.5 | | |
| 337.642 | $CH_3OH(7_{1,7} - 6_{1,6})E(v_t = 1)$ | 356 | 10.9[b] | 2.9[b] | 0.6[b] | 1.1[b] |
| 337.644 | $CH_3OH(7_{0,7} - 6_{0,6})E(v_t = 1)$ | 365 | 10.9[b] | 2.9[b] | 0.6[b] | 1.1[b] |
| 337.646 | $CH_3OH(7_{4,3} - 6_{4,2})E(v_t = 1)$ | 470 | 10.9[b] | 2.9[b] | 0.6[b] | 1.1[b] |
| 337.648 | $CH_3OH(7_{5,3} - 6_{5,2})E(v_t = 1)$ | 611 | 10.9[b] | 2.9[b] | 0.6[b] | 1.1[b] |
| 337.655 | $CH_3OH(7_{3,5} - 6_{3,4})A(v_t = 1)$ | 461 | 10.8[b] | 2.0[b] | | |
| | $CH_3OH(7_{3,4} - 6_{3,3})A^-(v_t = 1)$ | 461 | 10.8[b] | 2.0[b] | | |
| 337.671 | $CH_3OH(7_{2,6} - 6_{2,5})E(v_t = 1)$ | 465 | 10.2 | 2.1 | | |
| 337.686 | $CH_3OH(7_{4,3} - 6_{4,2})A(v_t = 1)$ | 546 | 9.[b]5 | 2.0[b] | | |
| | $CH_3OH(7_{4,4} - 6_{4,3})A^-(v_t = 1)$ | 546 | 9.5[b] | 2.0[b] | | |
| | $CH_3OH(7_{5,2} - 6_{5,1})E(v_t = 1)$ | 494 | 9.5[b] | 2.0[b] | | |
| 337.708 | $CH_3OH(7_{1,6} - 6_{1,5})E(v_t = 1)$ | 489 | 7.9 | 1.8 | | |
| 337.722 | $CH_3OCH_3(7_{4,4} - 6_{3,3})EE$ | 48 | | 0.9 | | |
| 337.732 | $CH_3OCH_3(7_{4,3} - 6_{3,3})EE$ | 48 | | 1.4 | | |
| 337.749 | $CH_3OH(7_{0,7} - 6_{0,6})A(v_t = 1)$ | 489 | 8.7 | 1.9 | | |
| 337.778 | $CH_3OCH_3(7_{4,4} - 6_{3,4})EE$ | 48 | | 1.3 | | |
| 337.787 | $CH_3OCH_3(7_{4,3} - 6_{3,4})AA$ | 48 | | 1.4 | | |
| 337.825 | $HC_3N(37 - 36)v_7 = 1$ | 629 | 14.8 | 1.4 | | |
| 337.838 | $CH_3OH(20_{6,14} - 21_{5,16})E$ | 676 | 5.6 | 1.1 | | |
| 337.878 | $CH_3OH(7_{1,6} - 6_{1,5})A(v_t = 2)$ | 748 | 2.7 | 0.6 | | |
| 337.969 | $CH_3OH(7_{1,6} - 6_{1,5})A(v_t = 1)$ | 390 | 12.0 | 2.1 | | |
| 338.081 | $H_2CS(10_{1,10} - 9_{1,9})$ | 102 | 5.8 | 2.3 | | 0.5 |
| 338.125 | $CH_3OH(7_{0,7} - 6_{0,6})E$ | 78 | 6.9 | 2.8 | 1.4 | 1.9 |
| 338.143 | $CH_3CH_2CN(37_{3,34} - 36_{3,33})$ | 317 | 14.4 | 0.9 | | |
| 338.214 | $CH_2CHCN(37_{1,37} - 36_{1,36})$ | 312 | 4.0 | | | |
| 338.306 | $SO_2(18_{4,1} - 18_{3,1})$ | 197 | $x$[c] | 0.8 | 1.2 | 0.7 |
| 338.345 | $CH_3OH(7_{1,7} - 6_{1,6})E$ | 71 | 13.4 | 2.1 | 1.3 | 2.3 |
| 338.405 | $CH_3OH(7_{6,2} - 6_{6,1})E$ | 244 | 13.1[b] | 3.0[b] | | |
| 338.409 | $CH_3OH(7_{0,7} - 6_{0,6})A$ | 65 | 13.1[b] | 3.0[b] | 1.5 | 2.4 |
| 338.431 | $CH_3OH(7_{6,1} - 6_{6,0})E$ | 254 | 9.5 | 1.8 | | |
| 338.442 | $CH_3OH(7_{6,1} - 6_{6,0})A$ | 259 | 11.7[b] | 2.7[b] | | 0.5[b] |
| | $CH_3OH(7_{6,2} - 6_{6,1})A^-$ | 259 | 11.7[b] | 2.7[b] | | 0.5[b] |
| 338.457 | $CH_3OH(7_{5,2} - 6_{5,1})E$ | 189 | 8.9 | 2.0 | 0.4 | 0.6 |
| 338.475 | $CH_3OH(7_{5,3} - 6_{5,2})E$ | 201 | 12.6 | 2.5 | 0.5 | |
| 338.486 | $CH_3OH(7_{5,3} - 6_{5,2})A$ | 203 | 9.4[b] | 2.3[b] | 0.8[b] | 0.8[b] |
| | $CH_3OH(7_{5,2} - 6_{5,1})A^-$ | 203 | 9.4[b] | 2.3[b] | 0.8[b] | 0.8[b] |
| 338.504 | $CH_3OH(7_{4,4} - 6_{4,3})E$ | 153 | 8.5 | 2.7 | 0.7 | 0.7 |
| 338.513 | $CH_3OH(7_{4,4} - 6_{4,3})A^-$ | 145 | 13.7[b] | 2.8[b] | 1.4[b] | 1.3[b] |
| | $CH_3OH(7_{4,3} - 6_{4,2})A$ | 145 | 13.7[b] | 2.8[b] | 1.4[b] | 1.3[b] |
| | $CH_3OH(7_{2,6} - 6_{2,5})A^-$ | 103 | 13.7[b] | 2.8[b] | 1.4[b] | 1.3[b] |
| 338.530 | $CH_3OH(7_{4,3} - 6_{4,2})E$ | 161 | 5.8 | 2.7 | 0.7 | 0.9 |
| 338.541 | $CH_3OH(7_{3,5} - 6_{3,4})A^+$ | 115 | 12.5[b] | 3.0[b] | 2.0[b] | 1.4[b] |
| 338.543 | $CH_3OH(7_{3,4} - 6_{3,3})A^-$ | 115 | 12.5[b] | 3.0[b] | 2.0[b] | 1.4[b] |

**Table 4**
(Continued)

| Freq. (GHz) | Line | $E_u/k$ (K) | $S_{peak}$ (Jy) Orion | $S_{peak}$ (Jy) G29.96 | $S_{peak}$ (Jy) 23151 | $S_{peak}$ (Jy) 05358 |
|---|---|---|---|---|---|---|
| 338.560 | $CH_3OH(7_{3,5} - 6_{3,4})E$ | 128 | 15.6 | 2.5 | 0.9 | 0.6 |
| 338.583 | $CH_3OH(7_{3,4} - 6_{3,3})E$ | 113 | 11.5 | 3.4 | 1.0 | 1.1 |
| 338.612 | $SO_2(20_{1,19} - 19_{2,18})$ | 199 | $x$[c] | 2.9 | 1.5 | 1.9 |
| 338.615 | $CH_3OH(7_{1,6} - 6_{1,5})E$ | 86 | $x$[d] | 2.9[d] | 1.5[d] | 1.9[d] |
| 338.640 | $CH_3OH(7_{2,5} - 6_{2,4})A$ | 103 | 7.2 | 2.5 | 1.0 | 1.0 |
| 338.722 | $CH_3OH(7_{2,5} - 6_{2,4})E$ | 87 | 10.2[b] | 3.2[b] | 2.1[b] | 2.7[b] |
| 338.723 | $CH_3OH(7_{2,6} - 6_{2,5})E$ | 91 | 10.2[b] | 3.2[b] | 2.1[b] | 2.7[b] |
| 338.760 | $^{13}CH_3OH(13_{7,7} - 12_{7,6})A$ | 206 | 4.0 | 1.1 | | |
| 338.769 | $HC_3N(37 - 36)v_7 = 2$ | 525 | ? | ? | | |
| 338.786 | $^{34}SO_2(14_{4,10} - 14_{3,1})$ | 134 | 6.2 | | | |
| 338.886 | $C_2H_5OH(15_{7,8} - 15_{6,19})$ | 162 | 5.3 | 0.8 | | |
| 338.930 | $^{30}SiO(8–7)$ | 73 | 24.4 | | | |
| 339.058 | $C_2H_5OH(14_{7,7} - 14_{6,8})$ | 150 | $x$[e] | 0.6 | | |
| 347.232 | $CH_2CHCN(38_{1,38} - 37_{1,37})$ | 329 | 4.9 | 0.6 | | |
| 347.331 | $^{28}SiO(8–7)$ | 75 | 22.1 | 0.9 | 0.7 | |
| 347.438 | UL | | 7.5 | | | |
| 347.446 | UL | | 3.4 | 0.8 | | |
| 347.478 | $HCOOCH_3(27_{1,26} - 26_{1,25})E$ | 247 | 4.8 | | | |
| 347.494 | $HCOOCH_3(27_{5,22} - 26_{5,21})A$ | 247 | 2.9 | 0.6 | | |
| 347.590 | $HCOOCH_3(16_{6,10} - 15_{5,11})A$ | 104 | 2.4 | | | |
| 347.599 | $HCOOCH_3(16_{6,10} - 15_{5,11})E$ | 105 | 1.7 | | | |
| 347.617 | $HCOOCH_3(28_{10,19} - 27_{10,18})A$ | 307 | 2.6 | | | |
| 347.628 | $HCOOCH_3(28_{10,19} - 27_{10,18})E$ | 307 | 3.6 | | | |
| 347.667 | UL | | 4.5 | | | |
| 347.759 | $CH_2CHCN(36_{2,34} - 35_{2,32})$ | 317 | 8.3 | 0.7 | | |
| 347.792 | UL | | 5.4 | 0.7 | | |
| 347.842 | UL, $^{13}CH_3OH$ | | 3.1 | 0.5 | | |
| 347.916 | $C_2H_5OH(20_{4,17} - 19_{4,16})$ | 251 | 3.3 | 0.7 | | |
| 347.983 | UL | | | 0.6 | | |
| 348.050 | $HCOOCH_3(28_{4,24} - 27_{4,23})E$ | 266 | 2.8 | | | |
| 348.066 | $HCOOCH_3(28_{6,23} - 27_{6,22})A$ | 266 | 3.0 | | | |
| 348.118 | $^{34}SO_2(19_{4,16} - 19_{3,17})$ | 213 | 5.8 | | | |
| 348.261 | $CH_3CH_2CN(39_{2,37} - 38_{2,36})$ | 344 | 11.2 | 1.2 | | |
| 348.340 | $HN^{13}C(4–3)$ | 42 | 16.1[b] | 2.0[b] | | |
| 348.345 | $CH_3CH_2CN(40_{2,39} - 39_{2,38})$ | 351 | 16.1[b] | 2.0[b] | | |
| 348.388 | $SO_2(24_{2,22} - 23_{3,21})$ | 293 | 9.3 | 0.5 | 1.0 | |
| 348.518 | UL, $HNOS(1_{1,1} - 2_{0,2})$ | | 10.6 | 0.7 | | |
| 348.532 | $H_2CS(10_{1,9} - 9_{1,8})$ | 105 | 7.4 | 1.9 | | |
| 348.553 | $CH_3CH_2CN(40_{1,39} - 39_{1,38})$ | 351 | 20.1 | | | |
| 348.910 | $HCOOCH_3(28_{9,20} - 27_{9,19})E$ | 295 | 11.0[b] | 1.6[b] | | |
| 348.911 | $CH_3CN(19_9 - 18_9)$ | 745 | 11.0[b] | 1.6[b] | | |
| 348.991 | $CH_2CHCN(37_{1,36} - 36_{1,35})$ | 325 | 5.9 | | | |
| 349.025 | $CH_3CN(19_8 - 18_8)$ | 624 | 9.5 | 1.1 | | |
| 349.107 | $CH_3OH(14_{1,13} - 14_{0,14})$ | 43 | 12.2 | 3.1 | 1.3 | 1.1 |

**Notes.**
[a] Doubtful detection since other close $v_t = 2$ lines with similar upper energy levels were not detected.
[b] Line blend.
[c] No flux measurement possible because averaged over the given 5700 AU negative features due to missing short spacings overwhelm the positive features (see Figures 3 and 6).
[d] Peak flux corrupted by neighboring $SO_2$ line.
[e] Only detectable with higher spatial resolution (Beuther et al. 2005a).

### *3.2.4. Sulfur Chemistry*

The rare carbon–sulfur isotopologue $C^{34}S$ is detected toward all the four regions (Figure 2). However, as shown in Figure 5, $C^{34}S$ does not peak toward the main submm continuum peaks but is offset at the edge of the core. In the cases of G29.96 and IRAS 23151+5912, the $C^{34}S$ morphology appears to wrap around the main submm continuum peaks. Toward IRAS 05358+3543, $C^{34}S$ is also weak toward the strongest submm peak (at the eastern edge of the image) but shows the strongest $C^{34}S$ emission features offset from a secondary submm continuum source (in the middle of the image). Toward Orion-KL, weak $C^{34}S$ emission is detected in the vicinity of the hot-core peak, whereas we find strong $C^{34}S$ emission peaks offset from the dust continuum emission.

To check whether our optical-thin assumption from Section 3.2.2 is valid also for $C^{34}S$, we ran LVG radiative transfer models (RADEX; van der Tak et al. 2007). We started with

**Table 5**
Molecular Column Densities

| | Orion-KL[a] | G29.96 | 23151 | 05358 |
|---|---|---|---|---|
| $CH_3OH$ | $2 \times 10^{16}$ | $4 \times 10^{17}$[b] | $3 \times 10^{16} - 1 \times 10^{17}$[c] | $4 \times 10^{15} - 4 \times 10^{18}$[d] |
| $CH_3CH_2CN$ | $5 \times 10^{15}$ | $1 \times 10^{16}$ | ... | ... |
| $CH_2CHCN$ | $5 \times 10^{15}$ | $7 \times 10^{15}$ | ... | ... |
| $C^{34}S$ | $2 \times 10^{14}$ | $2 \times 10^{15}$ | $2 \times 10^{14}$ | $6 \times 10^{13}$ |
| $CH_3OCH_3$ | $1 \times 10^{16}$ | $2 \times 10^{17}$[e] | ... | ... |
| $HCOOCH_3$ | $6 \times 10^{15}$ | $8 \times 10^{16}$ | ... | ... |
| $^{34}SO$ | $6 \times 10^{14}$ | $1 \times 10^{16}$ | $4 \times 10^{15}$ | ... |
| $SO_2$ | $2 \times 10^{15}$ | $3 \times 10^{16}$ | $3 \times 10^{16}$ | $1 \times 10^{16}$[d] |
| $HC_3N$ | $6 \times 10^{14}$ | $2 \times 10^{15}$ | ... | ... |
| $HN^{13}C$ | blend | blend | ... | ... |
| $H_2CS$ | $4 \times 10^{14}$ | $2 \times 10^{16}$ | ... | $4 \times 10^{14}$ |
| $C_2H_5OH$ | $2 \times 10^{15}$ | $6 \times 10^{16}$ | ... | ... |
| SiO | $2 \times 10^{14}$ | $4 \times 10^{14}$ | $2 \times 10^{14}$ | ... |
| $CH_3CN$ | $2 \times 10^{15}$ | $1 \times 10^{16}$ | ... | $8 \times 10^{16}$[d] |

**Notes.**
[a] Calculated for a lower average $T$ of 200 K because of smoothing to 5700 AU resolution (Figures 2 and 3). The source size was approximated by half the spatial resolution. The on average lower Orion-KL column densities are likely due to the largest amount of missing flux for the closest source of the sample.
[b] From Beuther et al. (2007c).
[c] From Beuther et al. (2007d) for different subsources.
[d] From Leurini et al. (2007) for different subsources.
[e] At lower temperature of 100 K, because otherwise different lines would get excited.

the $H_2$ column densities from Table 1 and assumed a typical $CS/H_2$ abundance of $10^{-8}$ with a terrestrial $CS/C^{34}S$ ratio of 23 (Wannier 1980). Above the critical density of $2 \times 10^7$ $cm^{-3}$, with the given broad $C^{34}S$ spectral FWHM (between 5 and 12 km $s^{-1}$ for the four sources), the $C^{34}S(7–6)$ emission is indeed optically thin. Hence, optical depth effects are not causing these large offsets. Since, furthermore, the line intensities depend not just on the excitation but also more strongly on the gas column densities, excitation effects only, as quantified in Section 3.2.1, cannot cause the observational offsets as well. Therefore, chemical evolution may be more important. A likely scenario is based on different desorption temperatures of molecules from dust grains (e.g., Viti et al. 2004): CS and $C^{34}S$ are desorbed from grains at temperatures of a few 10 K, and at such temperatures, these molecules are expected to be well correlated with the dust continuum emission. Warming up further, at 100 K $H_2O$ desorbs and then dissociates to OH. The OH quickly reacts with the sulfur forming SO and $SO_2$ which then will be centrally peaked (see Section 3.2.6). Toward G29.96, IRAS 23151+5912, and IRAS 05358+3543, we find that the $SO_2$ emission is centrally peaked toward the main submm continuum peaks, confirming the above-outlined chemical scenario (Figure 6 & Section 3.2.6[5]). To further investigate the $C^{34}S/SO_2$ differences, we produced column density ratio maps between $C^{34}S$ and $SO_2$ for G29.96, IRAS 23151+5912, and IRAS 05358+3543, assuming local thermodynamic equilibrium and optically-thin emission (Figure 7). To account for the spatial differences that $SO_2$ is observed toward the submm peak positions whereas $C^{34}S$ is seen more to the edges of the cores, for the column density calculations, we assumed the temperatures given in Table 1 for $SO_2$, whereas we used half that temperature for $C^{34}S$. Although the absolute ratio values are highly uncertain because of the different spatial filtering properties of the two molecules, qualitatively as expected, the column density ratio maps have the lowest values in the vicinity of the submm continuum sources and show increased emission at the core edges. The case is less clear for Orion-KL which shows the strongest $SO_2$ emission toward the southeastern region called compact ridge. Since this compact ridge is believed to be caused by the interaction of a molecular outflow with the ambient dense gas (e.g., Liu et al. 2002) and $SO_2$ is known to be enriched by shock interactions with outflows, this shock-outflow interaction may dominate in Orion-KL compared with the above-discussed $C^{34}S/SO_2$ scenario. For more details on the chemical evolution, see the modeling in Section 3.2.6.

[5] For G29.96, the $SO_2$ peaks are actually right between the better resolved submm continuum sources. This is due to the lower resolution of the line data because smoothing the continuum to the same spatial resolution, they peak very close to the $SO_2$ emission peaks (see e.g., Figure 2 in Beuther et al. 2007c).

#### *3.2.5. Nitrogen Chemistry*

It is intriguing that we do not detect any nitrogen-bearing molecule toward the two younger HMPOs IRAS 23151+5912 and IRAS 05358+3543 (Figure 2 and Table 4). This already indicates that the nitrogen-chemistry needs warmer gas to initiate or requires more time to proceed. To get an idea about the more subtle variations of the nitrogen chemistry, one may compare some specific line pairs: for example, the $HN^{13}C/CH_3CH_2CN$ line blend (dominated by $HN^{13}C$) and the $SO_2$ line between 348.3 and 348.4 GHz are of similar strength in the HMC Orion-KL (Figure 2). The same is approximately true for the HMC G29.96, although $SO_2$ is relatively speaking a bit weaker there. The more interesting differences arise if one contrasts with the younger sources. Toward the $10^5$ $L_\odot$ early HMPO IRAS 23151+5912, we only detect the $SO_2$ line, and the $HN^{13}C/CH_3CH_2CN$ line blend remains a non-detection in this source. In the lower luminosity early HMPO IRAS 05358+3543, both lines are not detected, although another $SO_2$ line at 338.3 GHz is detected there.

Judging from these line ratios, one can infer that $SO_2$ is relatively easy to excite early on in the evolution of high-mass star-forming regions. Other sulfur-bearing molecules like $H_2CS$ or CS are released even earlier from the grains, but

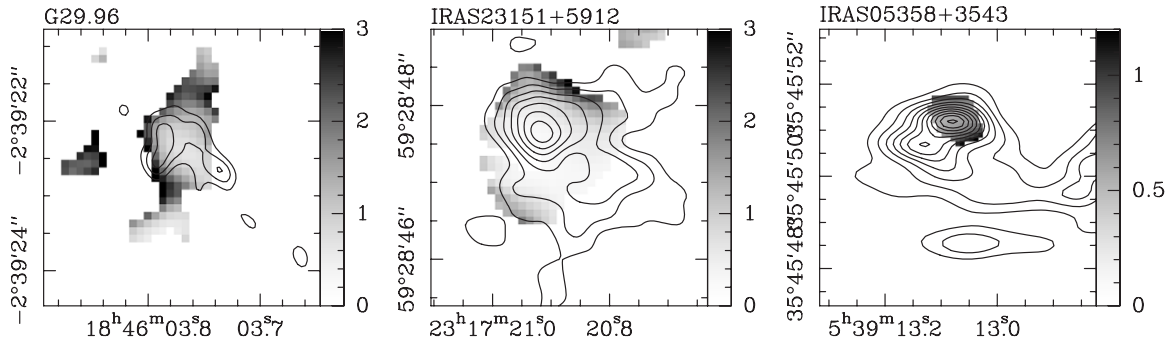


**Figure 7.** Column density ratios between $C^{34}S$ over $SO_2$ toward G29.96, IRAS 23151+5912 and IRAS 05358+3543 are shown in gray scale. The contours present the corresponding submm continuum maps as in shown the previous figures. For IRAS 05358+3543 we zoom only into the central region to better show the ratio variations.

SO-type molecules are formed quickly (e.g., Charnley 1997; Nomura & Millar 2004). In contrast to this, the non-detection of spectral lines like the $HN^{13}C/CH_3CH_2CN$ line blend in the early HMPOs indicates that the formation and excitation of such nitrogen-bearing species takes place in an evolutionary more evolved phase. This may either be due to molecule-selective temperature-dependent gas–dust desorption processes or chemical network reactions requiring higher temperatures. Furthermore, simulations of chemical networks show that the complex nitrogen chemistry simply needs more time to be activated (e.g., Charnley et al. 2001; Nomura & Millar 2004). Recent modeling by Garrod et al. (2007) indicates that the gradual switch-on phase of hot molecular cores is an important evolutionary stage to produce complex molecules. In this picture, the HMCs have switched on their heating sources earlier and hence had more time to form these nitrogen molecules.

Comparing just the two HMCs, we find that the $CH_3CH_2CN$ at 348.55 GHz is strong in Orion-KL but not detected in G29.96. Since G29.96 also exhibits less vibrationally torsionally excited $CH_3OH$ lines, it is likely on average still at lower temperatures than Orion-KL and may hence have not formed yet all the complex nitrogen-bearing molecules present already in Orion-KL.

### *3.2.6. Modeling*

To examine the chemical evolution of warm regions in more detail, we used the chemical model of Bergin & Langer (1997). This model includes gas-phase chemistry and the freeze-out to and sublimation from grain surfaces. The details of this model are provided in that paper with the only addition being the inclusion of water ice formation on grain surfaces. The binding energies we have adopted are for bare silicate grains, except for water ice, which is assumed to have a binding energy appropriate for hydrogen bonding between frozen water molecules (Fraser et al. 2001). To explore the chemistry of these hot evaporative regions, we have run the model for $10^6$ yrs with starting conditions at $n_{H_2} = 10^6$ cm$^{-3}$ and $T_{gas} = T_{dust} = 20$ K. Under these conditions most gaseous molecules, excluding $H_2$, will freeze onto the grain surface and the ice mantle forms, dominated by $H_2O$. This timescale ($10^5$ yrs) is quite short, but is longer than the free-fall time at this density and is chosen as a representative time that gas might spend at very high density. After completion, we assume that a massive star forms and the gas and dust temperature is raised such that the ice mantle evaporates and the gas-phase chemistry readjusts. We have made one further adjustment to this model. Our data suggest that HNC (a representative nitrogen-bearing species) is not detected in early HMPOs and that the release of this species (or its precursor) from the ice occurs during more evolved and warmer stages. Laboratory data on ice desorption suggest that the process is not as simple as generally used in models where a given molecule evaporates at its sublimation temperature (Collings et al. 2004). Rather some species co-desorb with water ice and the key nitrogen-bearing species, $NH_3$, falls into this category (see also Viti et al. 2004). We have therefore assumed that the ammonia evaporates at the same temperature as water ice. Our initial abundances are taken from Aikawa et al. (1996), except we assume that 50% of the nitrogen is frozen in the form of $NH_3$ ice. This assumption is consistent with two sets of observations. First, detections of $NH_3$ in ices toward YSO's find abundances of $\sim$ 2%–7% relative to $H_2O$ (Bottinelli et al. 2007). Dartois et al. (2002) find a limit of $\sim$ 5% relative to $H_2O$ toward other YSO's. Our assumed abundance of $NH_3$ ice is $5 \times 10^{-6}$ relative to $H_2O$, assuming an ice abundance of $10^{-4}$ (as appropriate for cold sources); this provides an ammonia ice abundance of $\sim$5%, which is consistent with ice observations. Second, high-resolution ammonia observations often find high abundances of $NH_3$ in the gas phase toward hot cores, often as high as $10^{-5}$, relative to $H_2$ (e.g., Cesaroni et al. 1994). Pure gas phase chemistry will have some difficulty making this high abundance in the cold phase, and we therefore assume it is made on grains during cold phases.

Figure 8 presents our chemical model results at the point of star "turn on" where the gas and dust becomes warmer and ices evaporate. Two different models were explored. The first labeled as $T_{dust} = 70$ K ("warm model") is a model which is insufficient to evaporate water ice, while the second, "hot model" with $T_{dust} = 150$ K, evaporates the entire ice mantle. Much of the chemical variations among the early HMPO and HMC phases is found for CS, SO, $SO_2$, and HNC (note this line is blended with $CH_3CH_2CN$), and we focus on these species in our plots (along with $H_2O$). It is also important to reiterate that due to differences in spatial sampling among the different sources as well as between line and continuum emission, we cannot derive accurate abundances from these data, but rather can attempt to use the models to explain trends. For the warm model, the main result is that the imbalance created in the chemistry by the release of most species, with ammonia and water remaining as ices on the grains, leads to enhanced production of CS. Essentially, the removal of oxygen from the gas (excluding the O found in CO) allows for rapid CS production from the atomic sulfur frozen on grains during the cold phase. Thus, for early HMPOs, which might not have a large fraction of gas above the water sublimation point ($T \sim 110$ K), the ratios of CS to other species are quite large. In the hot model, when the temperature

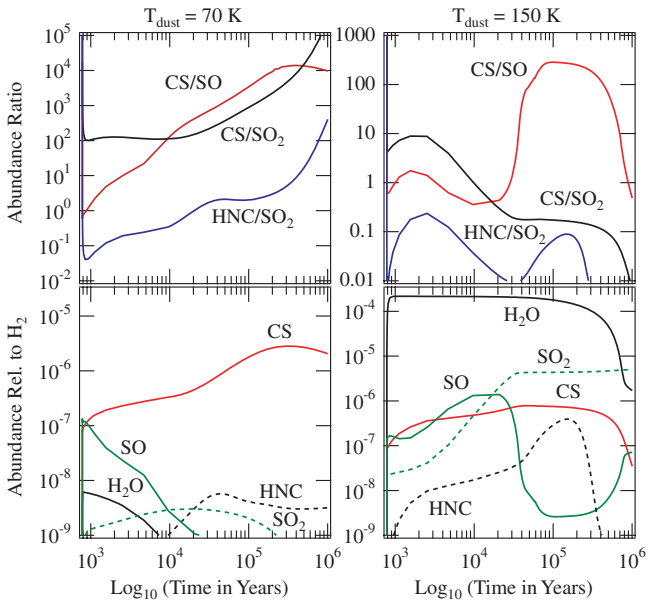


**Figure 8.** The left and right columns show results from our modeling of the "cold and warm models," respectively. The two top panels show the abundance ratios between several species important for our observations versus the time. The bottom panels present the abundances relative to $H_2$. Time in this figure refers to time after the onset of massive star formation and hence we do not show any evolution during the cold starless phase.

(A color version of this figure is available in the online journal.)

can evaporate both $H_2O$ and $NH_3$ ice, ratios between the same molecules are orders of magnitude lower (Figure 8). There is a large jump in the water vapor abundance (and $NH_3$, which is not shown) between the warm and the hot model, driving the chemistry into new directions. CS remains in the gas, but not with as high abundance as in the warm phase and is gradually eroded into SO and ultimately $SO_2$. Hence, $SO_2$ appears to be a better tracer of more evolved stages. In this sense, even the early HMPOs can be considered as relatively evolved, and it will be important to extend similar studies to even earlier evolutionary stages. HNC also appears as a brief intermediate product of the nitrogen chemistry.

The above picture is in qualitative agreement with our observations: that CS should be a good tracer in early evolutionary states even prior to our observed sample, but that it is less well suited for more evolved regions like those studied here. Other sulfur-bearing molecules, in particular $SO_2$, appear to better trace the warmest gas near the forming star. HNC and perhaps other nitrogen-bearing species are better tracers when the gas is warm enough to evaporate a significant amount of the ice mantle.

### *3.3. Searching for Disk Signatures*

While the chemical evolution of massive star-forming regions is interesting in itself, one also wants to use the different characteristics of molecular lines as tools to trace various physical processes. While molecules like CO or SiO have regularly been used to investigate molecular outflows (e.g., Arce et al. 2007), the problem to identify the right molecular tracer to investigate accretion disks in massive star formation is much more severe (e.g., Cesaroni et al. 2007). Major observational obstacles arise from the fact that disk-tracing molecular lines are usually often not unambiguously found only in the accretion disk, but that other processes can produce such line emission as well. For example, molecular lines from CN and HCN are high-density tracers and were believed to be good candidates to investigate disks in embedded protostellar sources (e.g., Aikawa & Herbst 2001). However, observations revealed that both

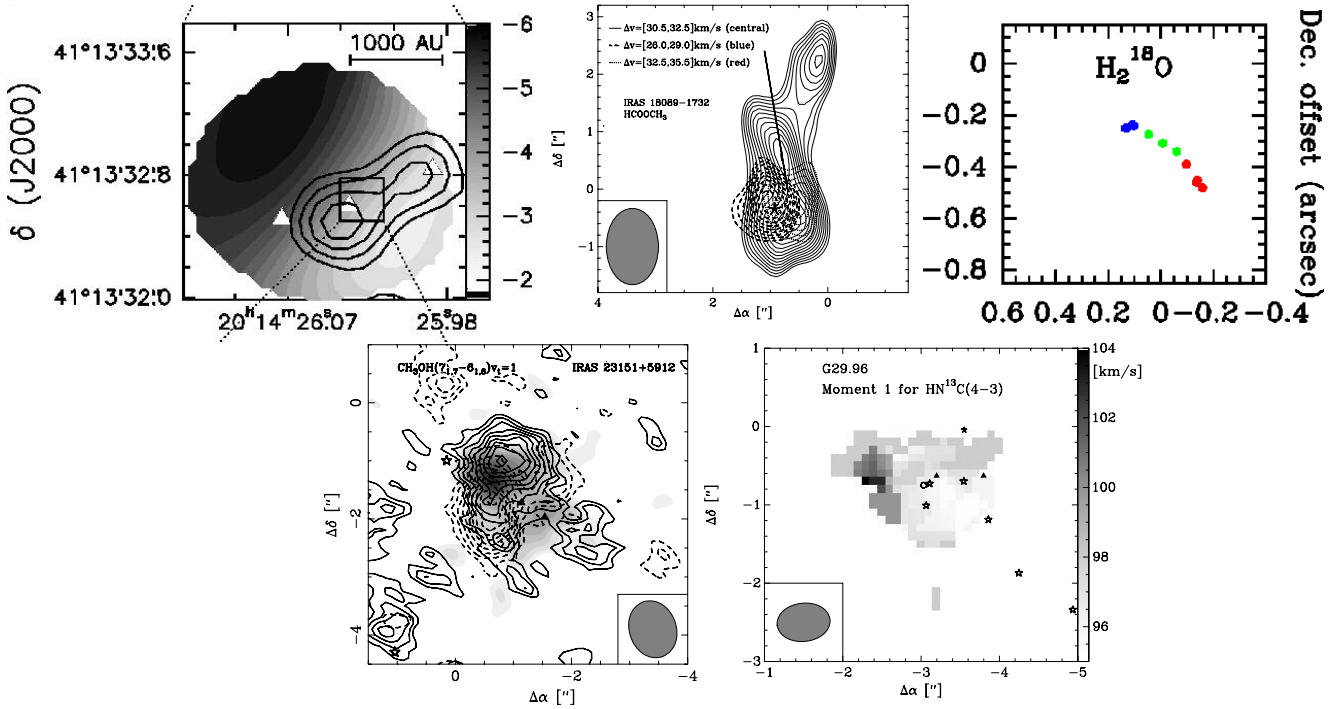


**Figure 9.** Examples of rotation-tracing molecules: top-left: $C^{34}S$ in IRAS 20126+4104 (Cesaroni et al. 1999, 2005), top-middle: $HCOOCH_3$ in IRAS 18089-1732 (Beuther et al. 2005b), top-right: $H_2^{18}O$ in AFGL2591 (van der Tak et al. 2006), bottom-left: $CH_3OH$ $v_t = 1$ in IRAS 23151+5912 (Beuther et al. 2007d), bottom-right: $HN^{13}C$ in G29.96 (Beuther et al. 2007c).

(A color version of this figure is available in the online journal.)

spectral lines are strongly affected by the associated molecular outflows and hence difficult to use for massive disk studies (CN Beuther et al. 2004a, HCN Zhang et al. 2007).

As presented in Cesaroni et al. (2007), various different molecules have in the past been used to investigate disks/rotational signatures in massive star formation (e.g., $CH_3CN$, $C^{34}S$, $NH_3$, $HCOOCH_3$, $C^{17}O$, $H_2^{18}O$, see also Figure 9). The data presented here add three other potential disk tracers ($HN^{13}C$ and $HC_3N$ for G29.96, Beuther et al. 2007c; and torsionally excited $CH_3OH$ for IRAS 23151+5912 and IRAS 05358+3543, Beuther et al. 2007d; Leurini et al. 2007; Figure 9). An important point to note is that in most sources only one or the other spectral line exclusively allows a study of rotational motions, whereas other lines apparently do not trace the warm disks. For example, $C^{34}S$ traces the Keplerian motion in the young source IRAS 20126+4104, whereas it does not trace the central protostars in the sources presented here (Figure 5). In contrast, $HN^{13}C$ shows rotational signatures in the HMC G29.96, but it remains completely undetected in the younger early HMPO sources of our sample (Figures 9 and 2). As discussed in Sections 3.2.4 and 3.2.5, this implies that depending on the chemical evolution molecules like $C^{34}S$ should be better suited for disk studies at very early evolutionary stages, whereas complex nitrogen-bearing molecules are promising in more evolved hot-core-type sources. While the chemical evolution is important for these molecules, temperature effects have to be taken into account as well. For example, the torsionally excited $CH_3OH$ line traces rotating motions in IRAS 23151+5912 and IRAS 05358+3543 (Beuther et al. 2007d; Leurini et al. 2007; Figure 9), but it is weak and difficult to detect in colder and younger sources. Therefore, some initial heating is required to employ highly excited lines for kinematic studies. In addition to these evolutionary effects, optical depth is important for many lines. For example, Cesaroni et al. (1997, 1999) have shown that $CH_3CN$ traces the rotating structure in IRAS 20126+4104, whereas the same molecule does not indicate any rotation in IRAS 18089-1732 (Beuther et al. 2005b). A likely explanation for the latter is high optical depth of the $CH_3CN$ submm lines (Beuther et al. 2005b). Again other molecules are excited in the accretion disks as well as the surrounding envelope, causing confusion problems to disentangle the various physical components. In summary, getting a chemical rich spectral line census like the ones presented here shows that one can find several disk-tracing molecules in different sources, but it also implies that some previously assumed good tracers are not necessarily universally useful.

The advent of broad bandpass interferometers like the SMA now fortunately allows us to observe many molecular lines simultaneously. This way, one often finds a suitable rotation-tracing molecule in an observational spectral setup. Nevertheless, one has to keep in mind the chemical and physical complexity in such regions, and it is likely that in many cases only combined modeling of infall, rotation and, outflow will disentangle the accretion disk from the rest of the star-forming gas and dust core.

## 4. CONCLUSION AND SUMMARY

We compiled a sample of four massive star-forming regions in different evolutionary stages with varying luminosities that were observed in exactly the same spectral setup at high-angular resolution with the SMA. We estimated column densities for all sources and detected species, and we compared the spatial distributions of the molecular gas. This allows us to start investigating chemical evolutionary effects also in a spatially resolved manner. Chemical modeling was conducted to explain our observations in more detail.

A general result from this comparison is that many different physical and chemical processes are important to produce the complex chemical signatures we observe. While some features, e.g., the nondetection of the rich vibrationally torsionally excited $CH_3OH$ line forest toward the two early HMPOs can be explained by on average lower temperatures of the molecular gas compared to the more evolved HMCs, other observational characteristics require chemical evolutionary sequences caused by heating including grain surface and gas phase reactions. Even other features are then better explained by shock-induced chemical networks.

The rare isotopologue $C^{34}S$ is usually not detected right toward the main submm continuum peaks, but rather at the edge of the star-forming cores. This may be explained by temperature-selective gas-desorption processes and successive gas chemistry networks. Furthermore, we find some nitrogen-bearing molecular lines to be only present in the HMCs, whereas they remain undetected at earlier evolutionary stages. This indicates that the formation and excitation of many nitrogen-bearing molecules needs considerably higher temperatures and/or more time during the warm-up phase of the HMC, perhaps relating to the fact that $NH_3$ is bonded within the water ice mantle. Although the statistical database is still too poor to set tighter constraints, these observations give the direction how one can use the presence *and* morphology of various molecular lines to identify and study different (chemical) evolutionary sequences.

Furthermore, we discussed the observational difficulty to unambiguously use one or the other spectral line as a tracer of massive accretion disks. While some early spectral line candidates are discarded for such kind of studies by now (e.g., CN), in many other sources we find different lines exhibiting rotational velocity signatures. The observational feature that in most sources apparently only one or the other spectral line exclusively traces the desired structures has likely to be attributed to a range of effects. (1) Chemical effects, where for example $C^{34}S$ may work in the youngest sources whereas some nitrogen-bearing molecules like $HN^{13}C$ are better in typical HMCs. (2) Confusion from multiple gas components, mainly outflows, infall from the envelope and rotation. (3) High optical depth from many molecular lines. This implies that for future statistical studies we have to select spectral setups that comprise many molecular lines from various species. This way, one has good chances to identify for each source separately the right molecular tracer, and hence still draw statistically significant conclusions.

To advance in this field and to become more quantitative, different steps are necessary. First of all, we need to establish a larger database of more sources at different evolutionary stages, in particular even younger sources, as well as with varying luminosities to better characterize the differences and similarities. From an observational and technical point of view, although the presented data are state of the art multiwavelength and high angular resolution observations, the quantitative interpretation is still hampered by the spatial filtering of the interferometer. To become more quantitative, it is therefore necessary to complement such data with the missing short spacing information. While we have high angular resolution in all datasets with a similar baseline coverage and hence similarly covered angular scales, the broad range of distances causes a different coverage

of sampled linear spatial scales. Hence, the missing short spacings affect each dataset in a different fashion which is currently the main limiting factor for a better quantitative interpretation of the data. Therefore, obtaining single-dish observations in the same spectral setup and then combining them with the SMA observations is a crucial step to derive more reliable column densities and; from that, abundances. These parameters then can be used by theorists to better model the chemical networks, explain the observations and predict other suitable molecules for, e.g., massive disk studies.

H.B. acknowledges financial support by the Emmy-Noether-Program of the Deutsche Forschungsgemeinschaft (DFG, grant BE2578).

## REFERENCES

Aikawa, Y., & Herbst, E. 2001, A&A, 371, 1107
Aikawa, Y., Miyama, S. M., Nakano, T., & Umebayashi, T. 1996, ApJ, 467, 684
Arce, H. G., et al. 2007, in Protostars and Planets V, ed. B. Reipurth, D. Jewitt, & K. Keil, 245
Bergin, E. A., & Langer, W. D. 1997, ApJ, 486, 316
Beuther, H., Churchwell, E. B., McKee, C. F., & Tan, J. C. 2007a, in Protostars and Planets V, ed. B. Reipurth, D. Jewitt, & K. Keil, 165
Beuther, H., Schilke, P., & Wyrowski, F. 2004a, ApJ, 615, 832
Beuther, H., Zhang, Q., Hunter, T. R., Sridharan, T. K., & Bergin, E. A. 2007d, A&A, 473, 493
Beuther, H., Zhang, Q., Sridharan, T. K., & Chen, Y. 2005b, ApJ, 628, 800
Beuther, H., et al. 2002a, A&A, 387, 931
Beuther, H., et al. 2002b, ApJ, 566, 945
Beuther, H., et al. 2004b, ApJ, 616, L31
Beuther, H., et al. 2005a, ApJ, 632, 355
Beuther, H., et al. 2007b, A&A, 466, 1065
Beuther, H., et al. 2007c, A&A, 468, 1045
Bisschop, S. E., Jørgensen, J. K., van Dishoeck, E. F., & de Wachter, E. B. M. 2007, A&A, 465, 913
Blake, G. A., Sutton, E. C., Masson, C. R., & Phillips, T. G. 1987, ApJ, 315, 621
Bottinelli, S., Boogert, A. C. A., van Dishoeck, E. F., Oberg, K., Pontoppidan, K. M., Blake, G. A., Evans, N. J., & Lahuis, F. 2007, in Molecules in Space and Laboratory, ed. J. L. Lemaire & F. Combes, 11
Brogan, C. L., Chandler, C. J., Hunter, T. R., Shirley, Y. L., & Sarma, A. P. 2007, ApJ, 660, L133
Cabrit, S., & Bertout, C. 1990, ApJ, 348, 530
Caselli, P., Hasegawa, T. I., & Herbst, E. 1993, ApJ, 408, 548
Cesaroni, R., Churchwell, E., Hofner, P., Walmsley, C. M., & Kurtz, S. 1994, A&A, 288, 903
Cesaroni, R., Felli, M., Testi, L., Walmsley, C. M., & Olmi, L. 1997, A&A, 325, 725
Cesaroni, R., Galli, D., Lodato, G., Walmsley, C. M., & Zhang, Q. 2007, in Protostars and Planets V, ed. B. Reipurth, D. Jewitt, & K. Keil (Tucson, AZ: Univ. Arizona Press), 197
Cesaroni, R., et al. 1999, A&A, 345, 949
Cesaroni, R., et al. 2005, A&A, 434, 1039
Charnley, S. B. 1997, ApJ, 481, 396
Charnley, S. B., Rodgers, S. D., & Ehrenfreund, P. 2001, A&A, 378, 1024
Collings, M. P., et al. 2004, MNRAS, 354, 1133
Dartois, E., d'Hendecourt, L., Thi, W., Pontoppidan, K. M., & van Dishoeck, E. F. 2002, A&A, 394, 1057
Doty, S. D., van Dishoeck, E. F., & Tan, J. C. 2006, A&A, 454, L5
Doty, S. D., van Dishoeck, E. F., van der Tak, F. F. S., & Boonman, A. M. S. 2002, A&A, 389, 446
Fraser, H. J., Collings, M. P., McCoustra, M. R. S., & Williams, D. A. 2001, MNRAS, 327, 1165
Garrod, R. T., Wakelam, V., & Herbst, E. 2007, A&A, 467, 1103
Hatchell, J., Thompson, M. A., Millar, T. J., & MacDonald, G. H. 1998, A&AS, 133, 29
Hildebrand, R. H. 1983, QJRAS, 24, 267
Ho, P. T. P., Moran, J. M., & Lo, K. Y. 2004, ApJ, 616, L1
Johnstone, D., Boonman, A. M. S., & van Dishoeck, E. F. 2003, A&A, 412, 157
Krumholz, M. R., Klein, R. I., & McKee, C. F. 2007, ApJ, 656, 959
Leurini, S., et al. 2007, A&A, 475, 925
Liu, S., Girart, J. M., Remijan, A., & Snyder, L. E. 2002, ApJ, 576, 255
Müller, H. S. P., Thorwirth, S., Roth, D. A., & Winnewisser, G. 2001, A&A, 370, L49
MacDonald, G. H., Gibb, A. G., Habing, R. J., & Millar, T. J. 1996, A&AS, 119, 333
McCutcheon, W. H., et al. 2000, MNRAS, 316, 152
Menten, K. M., & Reid, M. J. 1995, ApJ, 445, L157
Millar, T. J., MacDonald, G. H., & Gibb, A. G. 1997, A&A, 325, 1163
Mueller, K. E., Shirley, Y. L., Evans, N. J., & Jacobson, H. R. 2002, ApJS, 143, 469
Nomura, H., & Millar, T. J. 2004, A&A, 414, 409
Olmi, L., et al. 2003, A&A, 407, 225
Poynter, R. L., & Pickett, H. M. 1985, Appl. Opt., 24, 2235
Schilke, P., Groesbeck, T. D., Blake, G. A., & Phillips, T. G. 1997, ApJS, 108, 301
Sridharan, T. K., Beuther, H., Schilke, P., Menten, K. M., & Wyrowski, F. 2002, ApJ, 566, 931
Thompson, M. A., Hatchell, J., Walsh, A. J., MacDonald, G. H., & Millar, T. J. 2006, A&A, 453, 1003
van der Tak, F. F. S., Black, J. H., Schöier, F. L., Jansen, D. J., & van Dishoeck, E. F. 2007, A&A, 468, 627
van der Tak, F. F. S., Boonman, A. M. S., Braakman, R., & van Dishoeck, E. F. 2003, A&A, 412, 133
van der Tak, F. F. S., van Dishoeck, E. F., & Caselli, P. 2000, A&A, 361, 327
van der Tak, F. F. S., Walmsley, C. M., Herpin, F., & Ceccarelli, C. 2006, A&A, 447, 1011
van Dishoeck, E. F., & Blake, G. A. 1998, ARA&A, 36, 317
Viti, S., Collings, M. P., Dever, J. W., McCoustra, M. R. S., & Williams, D. A. 2004, MNRAS, 354, 1141
Wakelam, V., Selsis, F., Herbst, E., & Caselli, P. 2005, A&A, 444, 883
Wannier, P. G. 1980, ARA&A, 18, 399
Wright, M. C. H., Plambeck, R. L., & Wilner, D. J. 1996, ApJ, 469, 216
Wyrowski, F., Schilke, P., Walmsley, C. M., & Menten, K. M. 1999, ApJ, 514, L43
Yorke, H. W., & Sonnhalter, C. 2002, ApJ, 569, 846
Zhang, Q., et al. 2007, A&A, 470, 269
Zinnecker, H., & Yorke, H. W. 2007, ARA&A, 45, 481